PHYSICAL REVIEW B **86**, 024436 (2012)

Spin-dependent Seebeck coefficients of $Ni_{80}Fe_{20}$ and Co in nanopillar spin valves

F. K. Dejene,* J. Flipse, and B. J. van Wees

Physics of Nanodevices, Zernike Institute for Advanced Materials, University of Groningen, Groningen, The Netherlands

(Received 25 May 2012; published 27 July 2012)

We have experimentally determined the spin-dependent Seebeck coefficient of permalloy ($Ni_{80}Fe_{20}$) and cobalt (Co) using nanopillar spin valve devices, a stack of two ferromagnetic layers separated by a nonmagnetic layer. The devices were specifically designed to separate heat-related effects from charge-related effects. A heat current, with no accompanying charge current, through the nanopillar spin valve leads to a thermovoltage proportional to the spin-dependent Seebeck coefficient $S_S = S_\uparrow - S_\downarrow$ of the ferromagnet, where $S_\uparrow$ and $S_\downarrow$ are the Seebeck coefficient for spin-up and spin-down electrons. By using a three-dimensional finite-element model based on spin-dependent thermoelectric theory, whose input material parameters were measured in separate devices, we were able to accurately determine a spin-dependent Seebeck coefficient of $-1.8\ \mu V\ K^{-1}$ and $-4.5\ \mu V\ K^{-1}$ for cobalt and permalloy, respectively, corresponding to a Seebeck coefficient polarization $P_S = S_S/S_F$ of 0.08 and 0.25, where S_F is the Seebeck coefficient of the ferromagnet. The results are in agreement with earlier theoretical work in Co/Cu multilayers and spin-dependent Seebeck and spin-dependent Peltier measurements in $Ni_{80}Fe_{20}$/Cu spin valve structures.

DOI: 10.1103/PhysRevB.86.024436 PACS number(s): 72.15.Jf, 72.25.−b, 85.75.−d, 85.80.−b

I. INTRODUCTION

The interplay between spin and heat transport in magnetic structures is studied in the emerging field called spin caloritronics.[1,2] This subfield of spintronics has recently gained a lot of interest leading to notable experimental[3–8] and theoretical studies.[9,10] At the heart of spin caloritronics lie the spin-dependent Seebeck and the spin-dependent Peltier effects. In the spin-dependent Seebeck effect, due to the difference in the Seebeck coefficient of spin-up and spin-down electrons in a ferromagnetic metal, a pure heat current (with no accompanying charge current) through a ferromagnetic layer (F)/nonmagnetic layer (N) interface drives spin angular momentum (spin current) across the interface thereby creating a spin accumulation which is proportional to S_S. Slachter *et al.*[6] extracted a spin-dependent Seebeck coefficient S_S of $-3.8\ \mu V\ K^{-1}$ in $Ni_{80}Fe_{20}$/Cu lateral spin valve devices using a three-dimensional finite-element model (3D-FEM). Here it is important to point out the fundamental difference between the spin-dependent Seebeck effect and the so-called "spin Seebeck effect".[11] Whereas the spin-dependent Seebeck effect is purely electronic in nature, the latter is now understood to originate from collective effects involving nonequilibrium thermally induced spin pumping due to temperature differences between, for example, conduction electrons and magnons.[2,12]

The spin-dependent Peltier effect, which is the reciprocal of the spin-dependent Seebeck effect, describes heating/cooling of a F/N interface by a spin current. More recently, Flipse *et al.*[7] demonstrated the spin-dependent Peltier effect in $Ni_{80}Fe_{20}$/Cu/$Ni_{80}Fe_{20}$ nanopillar spin valve devices from which a spin-dependent Peltier coefficient Π_S of -1.1 mV was obtained. The spin-dependent Seebeck and Peltier coefficient reported in Refs. 6 and 7 follow the Thomson-Onsager relation $\Pi_S = S_S T_o$, where T_o is the temperature.

Although the concept of the spin dependency of the Seebeck coefficient was first discussed by Campbell *et al.*[13] and later used to explain large magnetothermoelectric powers in Co/Cu multilayers,[14–16] reports on the Seebeck coefficient polarization $P_S = S_S/S_F$ are relatively scarce. For $Ni_{80}Fe_{20}$, a P_S of 0.20 has been reported from spin-dependent Seebeck[6] and spin-dependent Peltier[7] measurements. In case of Co, effective P_S values ranging from 0.18[16,17] to 0.42[14,18] were reported from thermopower measurements in Co/Cu multilayers and diluted Co alloys, respectively. To quantify the size of spin caloritronic effects, one needs to accurately determine spin-dependent thermoelectric coefficients. In this paper, therefore, we provide absolute values of the spin-dependent Seebeck coefficient and its polarization for cobalt and permalloy from spin-dependent Seebeck measurements in F/N/F pillar spin valve devices.

The objectives of this paper are therefore twofold. First, it describes the spin-dependent Seebeck effect in specifically designed nanopillar spin valve devices. Second, it presents an accurate determination of the spin-dependent Seebeck coefficients for $Ni_{80}Fe_{20}$ and Co using a 3D-FEM. To that end, the electrical conductivity and Seebeck coefficient of all materials were measured in separate devices. The thermal conductivity of the thin metallic films was obtained from the measured electrical conductivity by using the Wiedemann-Franz law.[19] Thermal conductivity of insulating layers was determined from heat transport measurements across metal/insulator/metal structures.

This paper is organized as follows. In Sec. II, we present general spin-dependent thermoelectrics in the framework of the two spin-channel model and particularly explain thermally driven spin injection in symmetric F/N/F nanopillar devices. We also discuss the improvements to the 3D-FEM in terms of separately measuring the input material parameters. Section III presents details of the device fabrication and measurement schemes used in this study. Here we also explain how we achieve a temperature gradient over the F/N/F stack and present the two types of measurements that were performed to fully characterize the devices. Section IV presents the results of the electrical and thermal spin injection experiments and discusses how the polarization of the conductivity and of the Seebeck coefficient were extracted using the 3D-FEM. Finally, Section V presents the conclusions.

II. SPIN-DEPENDENT SEEBECK EFFECT IN F/N/F PILLAR SPIN VALVE

In metallic ferromagnets, charge, spin, and heat transport can be described by two parallel spin channels, one for spin-up (↑) and another for spin-down (↓) electrons, with each spin channel having its own conductivity $\sigma_{\uparrow,\downarrow}$ and Seebeck coefficient $S_{\uparrow,\downarrow}$.[13,20] The charge and heat current in each spin channel are related to their respective potential gradient $\vec{\nabla}\mu_{\uparrow,\downarrow}$ and temperature gradient $\vec{\nabla}T$ as[6]

$$\begin{pmatrix} \vec{J}_\uparrow \\ \vec{J}_\downarrow \\ \vec{Q} \end{pmatrix} = -\begin{pmatrix} \sigma_\uparrow & 0 & \sigma_\uparrow S_\uparrow \\ 0 & \sigma_\downarrow & \sigma_\downarrow S_\downarrow \\ \sigma_\uparrow \Pi_\uparrow & \sigma_\downarrow \Pi_\downarrow & k \end{pmatrix} \begin{pmatrix} \vec{\nabla}\mu_\uparrow/e \\ \vec{\nabla}\mu_\downarrow/e \\ \vec{\nabla}T \end{pmatrix}, \quad (1)$$

where $\Pi_{\uparrow,\downarrow}$ and $\mu_{\uparrow,\downarrow}$ are the Peltier coefficient and electrochemical potential for spin-up and spin-down electrons and κ is the thermal conductivity. Equation (1) is the basis for our 3D-FEM, which was previously used to describe spintronic and spin caloritronic phenomena. A detailed procedure for the modeling can be found in Ref. 21. By separately measuring the modeling parameters for each material in dedicated devices,[19] good agreement between the model and the measurement was obtained allowing us to accurately determine the spin-dependent Seebeck coefficients by using the measured electrical and thermal spin signals.

In the following, we describe the spin-dependent Seebeck effect in a symmetric F/N/F pillar stack with equal layer thicknesses ($t = 15$ nm) comparable to the spin relaxation length in the ferromagnet (λ_F) but much smaller than in the nonmagnetic layer ($\lambda_N = 300$ nm). In a ferromagnet, owing to the difference in the spin-dependent Seebeck coefficients $S_\uparrow \neq S_\downarrow$, a temperature gradient ∇T across a F/N interface drives a spin current $J_\uparrow - J_\downarrow$ from the F into the N region[6] thereby creating a nonequilibrium spin accumulation $\mu_s = \mu_\uparrow - \mu_\downarrow$, which is proportional to the spin-dependent Seebeck coefficient $S_S = S_\uparrow - S_\downarrow$ of the ferromagnet. Here, we define spin-up electrons as the spins with the higher conductivity, which in the case of both permalloy and cobalt are the majority spins. For a F/N/F pillar stack in a temperature gradient, thermal spin injection at the two F/N interfaces results in a spin accumulation in the N region that is a function of the relative alignment of the magnetization of the ferromagnets.

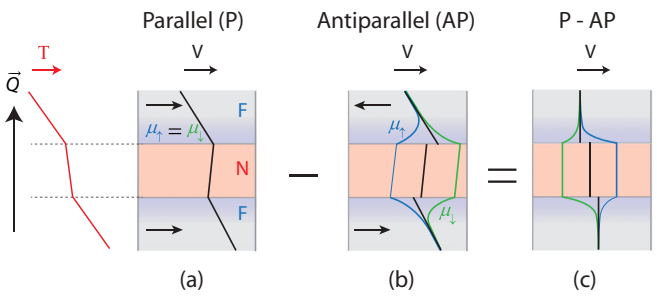

FIG. 1. (Color online) Spin electrochemical potentials $\mu_\uparrow$ (blue) and $\mu_\downarrow$ (green) in a F/N/F stack subjected to a temperature gradient in the case when the magnetizations are aligned (a) parallel and (b) antiparallel. (c) shows the difference between (a) and (b). The heat current and temperature profile are also shown to the left of (a).

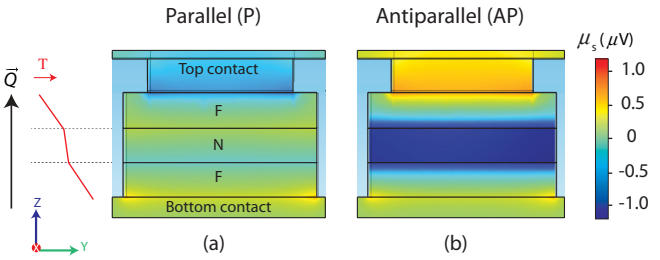

FIG. 2. (Color online) ZY-plane cross-section plot obtained from the 3D-FEM of the spin accumulation $\mu_s = \mu_\uparrow - \mu_\downarrow$ through the middle of a $Ni_{80}Fe_{20}$/Cu/$Ni_{80}Fe_{20}$ nanopillar for a temperature change $\Delta T = 7$ K across the the stack for the (a) parallel and (b) antiparallel configurations. The spin accumulation of –1 μV in (b) is significantly larger than in (a).

In the parallel (↑↑) configuration [Fig. 1(a)], spins are injected at the first interface while being extracted at the second resulting in a flow of constant spin current across the whole stack. This constant spin current flow dictates that there is negligible spin accumulation at the two F/N interfaces; that is, the individual spin chemical potentials $\mu_\uparrow$ and $\mu_\downarrow$ are equal. In the antiparallel configuration (↑↓), however, spins of similar kind are injected from both interfaces into the N region. In such configuration, the spin current in the bulk of the ferromagnets is opposite to each other giving rise to a large spin accumulation in the N region. This large spin accumulation results in the splitting of the spin electrochemical potentials [see Fig. 1(b)]. A cross-sectional plot of the spin accumulation μ_s obtained from the three-dimensional FEM (shown in Fig. 2) demonstrates the significant difference in the size of the spin accumulation for the two different configurations.

An expression for μ_s, based on a one-dimensional spin-diffusion equation, in the limit $t \gg \lambda_F, \lambda_N$, can be found elsewhere.[6,10] Here we extend this limit to devices with thicknesses t comparable to λ_F and λ_N and find the expression given in Eq. (B4) of the appendices, which is similar to the expression in Ref. 6 except for the resistance mismatch factor. The interfacial spin thermoelectric voltage drop $\Delta\mu = P_\sigma \mu_s$, which is different for the two configurations, can then be expressed as a function of the spin accumulation at the two F/N interfaces. In an experiment, one measures this open-circuit thermovoltage as a function of an external magnetic field. The spin valve signal $V_{SV} = (\Delta\mu^{\uparrow\uparrow} - \Delta\mu^{\uparrow\downarrow})/|e|$ is thus given by

$$V_{SV} = -2\lambda_F S_S \nabla T P_\sigma R_{\text{mismatch}}, \quad (2)$$

where ∇T is the temperature gradient in the F region and e is the electronic charge. The term R_{mismatch} denotes the resistance mismatch factor for a symmetric spin valve given by

$$R_{\text{mismatch}} = \frac{\cosh\left(\frac{t}{\lambda_F}\right) - \exp\left(-\frac{2t}{\lambda_F}\right)}{\frac{R_F}{R_N}\cosh\left(\frac{t}{\lambda_F}\right)\tanh\left(\frac{t}{2\lambda_N}\right) + \sinh\left(\frac{t}{\lambda_F}\right)}, \quad (3)$$

where $R_F = \lambda_F/(1 - P_\sigma^2)\sigma_F$ and $R_N = \lambda_N/\sigma_N$ are the spin resistances of the ferromagnet and the normal metal, respectively. In the limit $t \gg \lambda_F, \lambda_N$, R_{mismatch} reduces to the single F/N interface result which is often close to one. Note, however, that in the analysis we use the numerical results from the three-dimensional finite-element modeling based on Eq. (1) to extract P_σ and P_S.

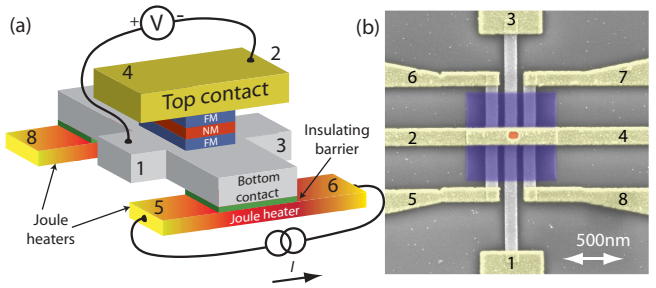

FIG. 3. (Color online) (a) Schematic representation of the measured device showing a F/N/F stack sandwiched between a Au-top contact (yellow) and Pt-bottom contact (gray). Platinum Joule heaters, which are electrically isolated from the bottom contact by an AlO_x barrier (green), are used to heat the bottom of the nanopillar. Homogeneous heating is achieved by two Pt Joule heaters on either side of the nanopillar. (b) Colored scanning electron microscope image of the measured device. Cross-linked PMMA matrix (blue) surrounding the pillar (red) is used to isolate the bottom contact from the top contact.

III. EXPERIMENTS

The nanopillar spin valve devices were prepared in one optical lithography step followed by nine electron-beam lithography (EBL) steps. Materials were deposited by e-beam evaporation at a base pressure of 2×10^{-6} Torr on a thermally oxidized Si substrate with a 300-nm-thick oxide layer. Figures 3(a) and 3(b) show a schematic and scanning electron microscope image of the measured device. The device consists of a F/N/F stack sandwiched between a bottom and top contact. The experimental methods and device fabrications are similar to the ones reported in Ref. 7.

First, a pair of 40-nm-thick Pt Joule heaters, which are 400 nm apart, were deposited. Then an 8-nm-thick AlO_x layer was deposited over the sides and surfaces of the Pt Joule heaters followed by the deposition of the bottom contact (60-nm-thick Pt). The AlO_x barriers electrically isolate the bottom contact from the Pt heaters to avoid charge-related effects. Then, the nanopillar spin valve with a structure F(15)/Cu(15)/F(15)/Au(10), where F = $Ni_{80}Fe_{20}$ or Co and the numbers between the parentheses are the thicknesses in nanometers, was deposited without breaking the vacuum of the deposition chamber to obtain clean interfaces. In the next two EBL steps, a top contact hole was defined followed by crosslinking a polymethyl methacrylate (PMMA) matrix around the nanopillar to isolate the bottom contact from the top contact. Finally, the top contact (130-nm-thick Au) was deposited.

The measurements presented in this paper are all performed at room temperature using standard lock-in techniques. A low-frequency ($f = 17$ Hz) ac current $I = I_0 \sin(2\pi f t)$ was used for the measurements to allow for efficient thermalization and a steady-state condition. To fully characterize the samples, two different measurements were performed. First, in the spin valve measurements, the four-probe resistance of the nanopillar was measured as a function of magnetic field. To that end, a 0.1 mA current was sent through the nanopillar from contact 3 to 4 while the voltage is measured using contacts 1 and 2. From the spin valve signal, the bulk spin polarization P_σ, which is later used in the determination of P_S, was extracted. In thermal spin injection measurements, the open-circuit voltage across the nanopillar was measured using contacts 1 and 2 while a current of 1 mA was sent through the Pt Joule heaters (contacts 5-6 and 7-8). The measured voltage was fed to two different lock-in amplifiers which were set to record the first harmonic $V^{(1f)} \propto I$ and second harmonic $V^{(2f)} \propto I^2$ responses of the signal. In the spin valve measurements, we looked at $V^{(1f)}$ while in the thermal spin injection measurements we were mainly interested in $V^{(2f)}$ since the spin-dependent Seebeck effect scales quadratically with the current through the Pt Joule heaters.[6,7,22]

IV. RESULTS AND DISCUSSION

Figure 4 shows the four-probe resistance $R^{(1f)} = V^{(1f)}/I$ measurements for $Ni_{80}Fe_{20}$ and Co nanopillar devices as a function of the in-plane magnetic field. The spin valve signal is defined as $R_s^{(1f)} = R^{\uparrow\uparrow} - R^{\uparrow\downarrow}$, where $R^{\uparrow\uparrow}$ and $R^{\uparrow\downarrow}$ are the resistance of the pillar in the parallel and antiparallel configurations, respectively. For $Ni_{80}Fe_{20}$ [Fig. 4(a)], a spin valve signal of -75 mΩ was observed on top of a background resistance, $R_b^{(1f)} = (R^{\uparrow\uparrow} + R^{\uparrow\downarrow})/2$, of 2.13 Ω. By using the measured spin signal as the only fitting parameter in the 3D-FEM, a conductivity polarization P_σ of 0.46 was extracted, which is in agreement with Andreev reflection measurements.[23] The calculated background resistance $R_b^{(1f)}$ of 1.77 Ω calculated with the finite-element model is in reasonable agreement with the measured background resistance.

The input parameters to the finite-element model, which are σ, S, κ, and Π, were all known from measurements in separate dedicated devices. The spin relaxation lengths λ_F for $Ni_{80}Fe_{20}$ and Co were obtained from Ref. 24. We used a spin relaxation length λ_F of 5 nm for $Ni_{80}Fe_{20}$ and 40 nm for Co, respectively. These values were systematically chosen by calculating the spin signal for different values of spin relaxation lengths and fitting it to the measured spin signals (see Fig. 8).

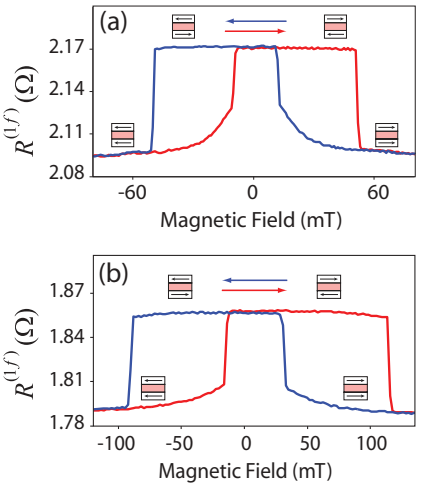

FIG. 4. (Color online) Spin valve resistance $V^{(1f)}/I$ for (a) $Ni_{80}Fe_{20}$ and (b) Co at a current of 0.1 mA. Magnetostatic or dipolar coupling between the two magnetizations in the nanopillar favors the AP configuration at zero magnetic field.

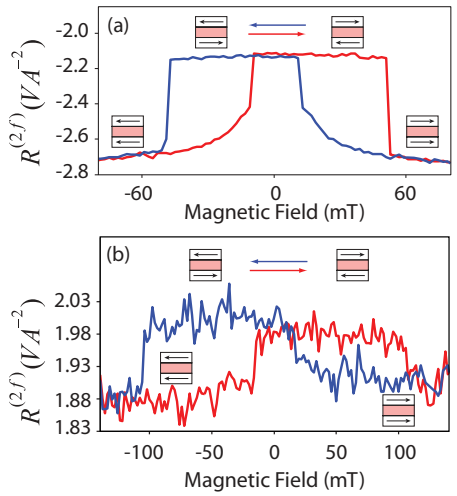

FIG. 5. (Color online) Spin-dependent Seebeck resistance $V^{(2f)}/I^2$ for (a) $Ni_{80}Fe_{20}$ and (b) Co at a current of 1 mA. Clear jumps in the measured voltage across the nanopillar occur at fields where the two magnetizations switch.

Following a similar analysis procedure for Co [Fig. 4(b)], from a spin signal $R_s^{(1f)}$ of -60 mΩ, we found a conductivity polarization $P_\sigma = 0.45$ in agreement with Andreev reflection measurements in metallic point contacts[23] and values reported elsewhere.[17] The background resistance, $R_b^{(1f)} = 1.82\ \Omega$, obtained from the measurement is a factor of two higher than the calculated background resistance of 0.99 Ω. This points to the presence of a possible interfacial resistance at the bottom Pt/Co or top Co/Au interfaces, which can effectively increase the resistance of the stack. Such resistive layer may arise, for example, from interfacial disorder due to some lattice mismatch and/or atomic or magnetic disorders.[25] If we account for such interfacial resistance, for a conductivity polarization $P_\sigma = 0.52$, we obtain a background resistance $R_b^{(1f)}$ of 1.5 Ω and a spin valve signal $R_s^{(1f)}$ of -56 mΩ in good agreement with the measurement.

Figure 5 shows the spin-dependent Seebeck measurements for a charge current of 1 mA through each Pt Joule heater (contacts 5 to 6 and 7 to 8) in opposite directions. The heat generated from the dissipated power in the Pt Joule heaters diffuses through the AlO_x insulating barrier and heats the bottom of the nanopillar thereby creating a temperature gradient over the stack. The temperature gradient across the pillar creates a Seebeck voltage $V^{(2f)}$ that depends on the relative orientation of the two magnetizations in the nanopillar.

For $Ni_{80}Fe_{20}$ [Fig. 5(a)], a spin-dependent Seebeck signal $R_s^{(2f)}$ of -0.6 V A^{-2} was measured on top of a background resistance $R_b^{(2f)} = -2.4$ V A^{-2}. From the measured spin signal, we obtain a spin-dependent Seebeck coefficient $S_S = S_\uparrow - S_\downarrow$ of $-4.5\ \mu$V K^{-1} corresponding to a Seebeck coefficient polarization $P_S = (S_\uparrow - S_\downarrow)/S_F$ of 0.25 in agreement with previous reports,[6,7] where $S_F = (\sigma_\uparrow S_\uparrow + \sigma_\downarrow S_\downarrow)/\sigma_F$.[6,7] The negative sign indicates that the Seebeck coefficient of spin-up electrons, which are the majority spins in $Ni_{80}Fe_{20}$ and Co, is more negative than that of the spin-down electrons. The calculated background resistance $R_b^{(2f)}$ of -2.43 V A^{-2} is in good agreement with the measured background resistance.

For cobalt [Fig. 5(b)], for a heating current of 1 mA, a spin signal $R_s^{(2f)}$ of -0.12 V A^{-2} was obtained. Similar analysis gives a spin-dependent Seebeck coefficient S_S of $-1.7\ \mu$V K^{-1} that corresponds to a Seebeck polarization $P_S = 0.07$. This result is comparable with a tight-binding calculation of the Seebeck coefficient of Co/Cu multilayers[26] where, from the energy derivative of σ and Mott's relation for the Seebeck coefficient, a Seebeck coefficient difference of $-1.76\ \mu$V K^{-1} between the parallel and antiparallel configurations was obtained. The measured background resistance $R_b^{(2f)}$ of 1.93 V A^{-2} is lower than the calculated $R_b^{(2f)}$ of 6.23 V A^{-2}. This discrepancy can be again attributed to the extra interfacial resistive layer that can modify the heat current (temperature profile) across the stack. Taking this interfacial thermal resistance in to account, we obtain a background resistance $R_b^{(2f)}$ of 2.4 V A^{-2} in good agreement with the measurement. The Seebeck coefficient polarization P_S of 0.14 obtained is however two times higher than that obtained without including the interfacial resistance ($P_S = 0.07$). In Fig. 5(b), there exists a visible asymmetry in the two parallel configurations due to possible contributions from the anomalous Nernst effect,[27] the thermal analog of the anomalous Hall effect. The transverse voltage resulting from the heat flow, which is proportional to the magnetization, is additive or subtractive depending on the orientation of the magnetization, causing an asymmetry.

TABLE I. Results of measurement on six other samples. The measured spin signals $R_s^{(1f)}$, $R_s^{(2f)}$, and background resistances $R_b^{(1f)}$, $R_b^{(2f)}$ are presented together with the calculated $R_{b,\mathrm{calc}}^{(1f)}$ and $R_{b,\mathrm{calc}}^{(2f)}$. The extracted polarization of the conductivity P_σ and the Seebeck coefficient P_S are also shown.

Sample	$R_s^{(1f)}$ (mΩ)	$R_s^{(2f)}$ (V A^{-2})	$R_b^{(1f)}$ (Ω)	$R_{b,\mathrm{calc}}^{(1f)}$ (Ω)	$R_b^{(2f)}$ (V A^{-2})	$R_{b,\mathrm{calc}}^{(2f)}$ (V A^{-2})	$P_\sigma = \frac{\sigma_\uparrow - \sigma_\downarrow}{\sigma_F}$	$P_S = \frac{S_\uparrow - S_\downarrow}{S_F}$	$S_\uparrow - S_\downarrow$ (μV K^{-1})
Py (Presented in main text)	-75	-0.60	2.12	1.77	-2.4	-2.43	0.46	0.25	-4.50
Py1	-61	-0.70	1.85	1.76	-4.0	-2.48	0.42	0.26	-4.68
Py2	-70	-0.60	2.26	1.76	-3.9	-2.43	0.45	0.25	-4.50
Py3	-80	-0.65	1.90	1.77	-4.0	-2.45	0.47	0.25	-4.50
Co (Presented in main text)	-60	-0.12	1.82	0.99	1.93	6.23	0.45	0.07	-1.68
Co1	-60	-0.12	1.89	0.99	1.64	6.23	0.45	0.07	-1.68
Co2	-62	-0.13	1.82	0.99	2.0	6.28	0.45	0.08	-1.92
Co3	-65	-0.12	1.83	1.02	1.95	6.23	0.46	0.07	-1.68

The results presented above were for two samples, one for $Ni_{80}Fe_{20}$ and one for Co, from a total of eight samples which were measured in a similar manner. Table I shows the measurement results of the remaining six samples. The polarization of the conductivity P_σ and Seebeck coefficient P_S were extracted by fitting the measured spin signals to the 3D-FEM. The modeled background resistances are in reasonably good agreement with the measurements and are consistent with the samples presented in the text.

V. CONCLUSION

In summary, we have performed all-electrical spin-dependent Seebeck effect measurements in $Ni_{80}Fe_{20}$ and Co nanopillar spin valve devices. We found that the polarization of the Seebeck coefficient for $Ni_{80}Fe_{20}$ (∼25%) and Co (∼8%) are in agreement with earlier experimental studies in $Ni_{80}Fe_{20}$/Cu spin valve structures and earlier theoretical works in Co/Cu multilayers, respectively. With the method presented here, it is in principle possible to measure the polarization of the conductivity and Seebeck coefficient of any ferromagnetic metal that makes up a symmetric or asymmetric spin valve.

ACKNOWLEDGMENTS

The authors thank B. Wolfs, M. de Roosz, and J. G. Holstein for technical assistance and N. Vlietstra for critically reading the manuscript. This work is part of the research program of the Foundation for Fundamental Research on Matter (FOM) and is supported by NanoLab NL, EU FP7 ICT (Grant No. 257159 MACALO) and the Zernike Institute for Advanced Materials.

APPENDIX A: TEMPERATURE PROFILE ACROSS F/N/F STACK

Figure 6 shows the temperature gradient and temperature profile of a symmetric F/N/F stack. From the 3D-FEM, for a heating current of 2 mA through the Pt Joule heaters, a temperature gradient up to 40 K μm^{-1} can be achieved in our devices [see Fig. 6(a)] corresponding to a $\Delta T = 8$ K across the F/N/F stack [see Fig. 6(b)]. The red line in Fig. 6(a) shows the temperature gradient across a $Ni_{80}Fe_{20}$/Cu/$Ni_{80}Fe_{20}$ pillar spin valve. From continuity of the heat current $\vec{Q} = -\kappa\vec{\nabla}T$ at the F/N interfaces, the temperature gradient in the ferromagnetic region ∇T_F is related to that of the N region ∇T_N as

$$\vec{\nabla}T_F = \frac{\kappa_N}{\kappa_F}\vec{\nabla}T_N, \tag{A1}$$

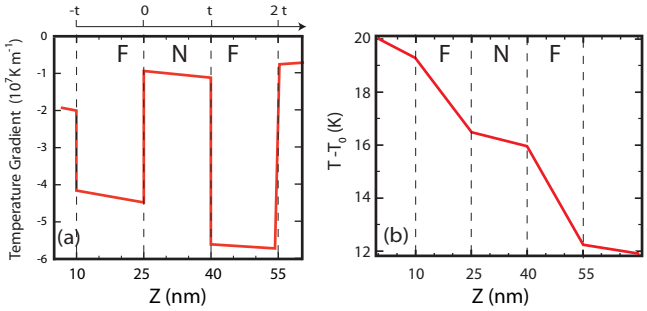

FIG. 6. (Color online) (a) Temperature gradient in a F/N/F pillar spin valve stack and (b) the temperature profile across the F/N/F stack for a heating current of 2 mA through both Joule heaters. For 1 mA current, the scale reduces by a factor of four.

where κ_F and κ_N are the thermal conductivity of the F and N regions, respectively.

APPENDIX B: EXPRESSION FOR THE SPIN ACCUMULATION

To obtain an expression for the spin accumulation $\mu_s = \mu_\uparrow - \mu_\downarrow$, we first need to solve the Valet-Fert 1D-spin diffusion equation $\partial^2(\mu_\uparrow - \mu_\downarrow)/\partial z^2 = (\mu_\uparrow - \mu_\downarrow)/\lambda_{sf}^2$ for each region in the F/N/F stack,[6] where λ_{sf} is the spin relaxation length. The general solution for each region reads
Region I ($-t < z < 0$):

$$\mu_{\uparrow,\downarrow} = A + Bz \pm \frac{C}{\sigma_{\uparrow,\downarrow}}e^{-z/\lambda_F} \pm \frac{D}{\sigma_{\uparrow,\downarrow}}e^{z/\lambda_F}, \tag{B1}$$

Region II ($0 < z < t$):

$$\mu_{\uparrow,\downarrow} = Fz \pm \frac{2G}{\sigma_N}e^{-z/\lambda_N} \pm \frac{2H}{\sigma_N}e^{z/\lambda_N}, \tag{B2}$$

Region III ($t < z < 2t$):

$$\mu_{\uparrow,\downarrow} = K + Lz \pm \frac{M}{\sigma_{\uparrow,\downarrow}}e^{-z/\lambda_F} \pm \frac{N}{\sigma_{\uparrow,\downarrow}}e^{z/\lambda_F}, \tag{B3}$$

where $+$ and $-$ denote the spin-up and spin-down, respectively, and λ_F and λ_N are the spin relaxation length in the F and N regions.

The spin accumulation μ_s at $z = 0$ and $z = t$ can then be expressed as a function of these coefficients as $\mu_s(z = 0) = \frac{4}{\sigma_N}(G + H)$ and $\mu_s(z = t) = \frac{4}{\sigma_N}(Ge^{-z} + He^{z})$, respectively. For a symmetric spin valve the spin accumulation, for example, at interface $z = 0$ for the $\uparrow\uparrow$ and $\uparrow\downarrow$ configurations reads

$$\mu_s^{\uparrow\uparrow}(z=0) = -e\lambda_F S_S \nabla T \frac{\left[\coth\left(\frac{t}{\lambda_N}\right) + \frac{\exp\left(-\frac{2t}{\lambda_F}\right)}{\sinh\left(\frac{t}{\lambda_N}\right)} - \tanh\left(\frac{t}{2\lambda_N}\right)\cosh\left(\frac{t}{\lambda_F}\right)\right]\frac{R_F}{R_N} + \left[-\sinh\left(\frac{t}{\lambda_F}\right) + \tanh\left(\frac{t}{\lambda_F}\right)\right]}{\cosh\left(\frac{t}{\lambda_F}\right)\left[\frac{R_F^2}{R_N^2} + 2\coth\left(\frac{t}{\lambda_N}\right)\tanh\left(\frac{t}{\lambda_F}\right)\frac{R_F}{R_N} + \tanh\left(\frac{t}{\lambda_F}\right)^2\right]}, \tag{B4}$$

$$\mu_s^{\uparrow\downarrow}(z=0) = -e\lambda_F S_S \nabla T \frac{\left[\coth\left(\frac{t}{\lambda_N}\right) + \frac{\exp\left(-\frac{2t}{\lambda_F}\right)}{\sinh\left(\frac{t}{\lambda_N}\right)} - \coth\left(\frac{t}{2\lambda_N}\right)\cosh\left(\frac{t}{\lambda_F}\right)\right]\frac{R_F}{R_N} + \left[-\sinh\left(\frac{t}{\lambda_F}\right) + \tanh\left(\frac{t}{\lambda_F}\right)\right]}{\cosh\left(\frac{t}{\lambda_F}\right)\left[\frac{R_F^2}{R_N^2} + 2\coth\left(\frac{t}{\lambda_N}\right)\tanh\left(\frac{t}{\lambda_F}\right)\frac{R_F}{R_N} + \tanh\left(\frac{t}{\lambda_F}\right)^2\right]}. \tag{B5}$$

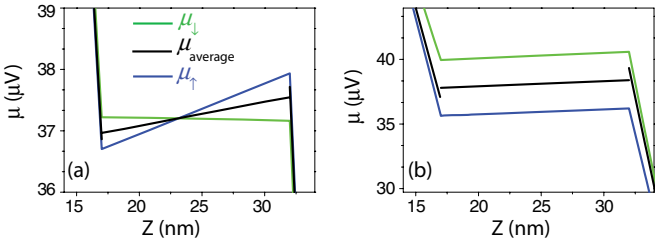

FIG. 7. (Color online) The electrochemical potential profile for spin-up $\mu_\uparrow$ and spin-down $\mu_\downarrow$ electrons and the average electrochemical potential $\mu_{\text{average}} = (\mu_\uparrow\sigma_\uparrow + \mu_\downarrow\sigma_\downarrow)/\sigma_F$ for (a) ↑↑ and (b) ↑↓ configurations.

In the limit $\lambda_N, \lambda_F \ll t$, Eq. (B5) reduces to the result obtained for a single F/N interface given in Refs. 6,10. Figure 7 shows the chemical potential profile across a F/N/F spin valve for the ↑↑ and ↑↓ configurations as obtained from the 3D-FEM. At the F/N interfaces, for both ↑↑ and ↑↓ configurations, a discontinuity in the average electrochemical potential μ_{average} leads to an electrochemical potential drop $\Delta\mu = P_\sigma \mu_s$. The spin valve signal V_{SV} is expressed in terms of these electrochemical potential drops as

$$V_{\text{SV}} = [(\Delta\mu^{\uparrow\uparrow}_{z=0} + \Delta\mu^{\uparrow\uparrow}_{z=t}) - (\Delta\mu^{\uparrow\downarrow}_{z=0} + \Delta\mu^{\uparrow\downarrow}_{z=t})]/|e|. \quad \text{(B6)}$$

APPENDIX C: MATERIAL PARAMETERS USED IN THE 3D-FEM

One important aspect of the finite-element modeling is good knowledge of the temperature and voltage profiles in the F/N/F pillar devices. This requires usage of appropriate material parameters in the 3D-FEM, which can often lead to underestimating background electrical and thermal voltages if bulk material parameters were used.[6,22] Table II shows material parameters used in the model. Electrical conductivity of each material was measured using a standard four-probe geometry. The thermal conductivity was then calculated using the Wiedemann-Franz law. For device dimensions discussed in the main text, the electronic contribution to the thermal conductivity is dominant over the lattice (phononic) conductivity.[19] The Seebeck coefficients were measured by using the technique presented in Ref. 19. One parameter which was not measured but obtained from the literature is the spin relaxation length λ_F of the ferromagnets. The spin relaxation length for $Ni_{80}Fe_{20}$ of 5 nm is well established in the literature.[24–28] However, the reported spin relaxation length of Co at room temperature varies from 20 nm to 60 nm.[24,28] The spin valve signals that are extracted from the model depend on the spin relaxation length and the polarization of the conductivity. To tackle the uncertainty in the spin relaxation length in Co, we performed a calculation of the spin signal for varying spin relaxation length values of the ferromagnet. Figure 8 shows the dependence of the spin signal on the spin relaxation length for different values of the conductivity polarization P_σ ranging between 0.42 and 0.47 (for $Ni_{80}Fe_{20}$) and 0.42 and 0.48 (for Co).

TABLE II. Material parameters used in finite-element modeling. The spin relaxation length λ_s was taken from various sources of literature (Refs. 24 and 28).

Material	t (nm)	σ (10^6 S m^{-1})	κ (W m^{-1} K^{-1})	S (μV K^{-1})	λ_s (nm)
$Ni_{80}Fe_{20}$	15	2.9	17	−18	5
Co	15	6.0	40	−22	40
Cu	15	15	10	1.6	300
Pt	40	4.2	32	−5	5
Pt	60	4.8	37	−5	3
Au	120	27	180	1.7	80
AlO_x	8	10^{-18}	0.12	0	
SiO_2	300	10^{-19}	1	0	

The shaded region in the figures indicates the region in which the measured spin signal values fall. For a choice of spin relaxation lengths of 5 nm (for $Ni_{80}Fe_{20}$) and 40 nm (for Co), the measured spin valve signals can be well fitted with the model. Hence, we used these two values for the determination of the spin-dependent Seebeck coefficients.

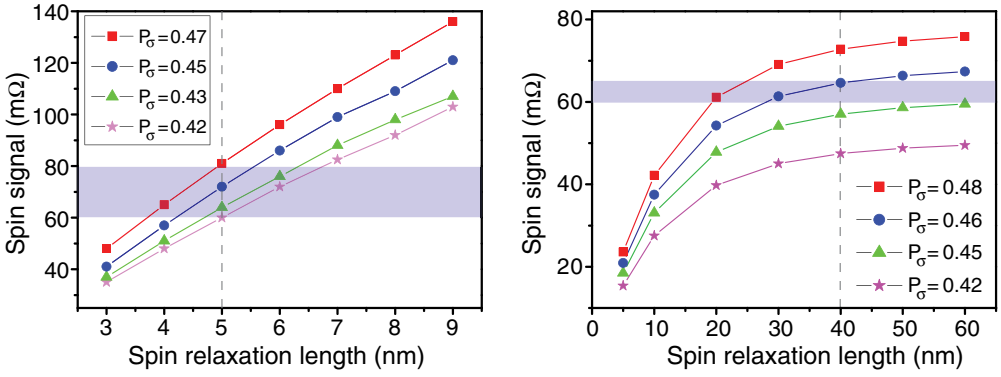

FIG. 8. (Color online) Dependence of the spin valve signal on the spin relaxation length λ_F of the FM for (a) $Ni_{80}Fe_{20}$/Cu/$Ni_{80}Fe_{20}$ and (b) Co/Cu/Co nanopillar spin valves. A λ_F of 5 nm for $Ni_{80}Fe_{20}$ and 40 nm for Co fits the measured spin signal, shown by the shaded region.

*f.k.dejene@rug.nl

[1] G. E. Bauer, A. H. MacDonald, and S. Maekawa, Solid State Commun. **150**, 459 (2010).

[2] G. E. W. Bauer, E. Saitoh, and B. J. van Wees, Nat. Mater. **11**, 391 (2012).

[3] K. Uchida, S. Takahashi, K. Harii, J. Ieda, W. Koshibae, K. Ando, S. Maekawa, and E. Saitoh, Nature (London) **455**, 778 (2008).

[4] J.-C. Le Breton, S. Sharma, H. Saito, S. Yuasa, and R. Jansen, Nature (London) **475**, 82 (2011).

[5] M. Walter, J. Walowski, V. Zbarsky, M. Münzenberg, M. Schäfers, D. Ebke, G. Reiss, A. Thomas, P. Peretzki, M. Seibt, J. S. Moodera, M. Czerner, M. Bachmann, and C. Heiliger, Nat. Mater. **10**, 742 (2011).

[6] A. Slachter, F. L. Bakker, J.-P. Adam, and B. J. van Wees, Nat. Phys. **6**, 879 (2010).

[7] J. Flipse, F. L. Bakker, A. Slachter, F. K. Dejene, and B. J. van Wees, Nat. Nanotechnol. **7**, 166 (2012).

[8] H. Yu, S. Granville, D. P. Yu, and J.-P. Ansermet, Phys. Rev. Lett. **104**, 146601 (2010).

[9] M. Hatami, G. E. W. Bauer, Q. Zhang, and P. J. Kelly, Phys. Rev. B **79**, 174426 (2009).

[10] B. Scharf, A. Matos-Abiague, I. Zutic, and J. Fabian, Phys. Rev. B **85**, 085208 (2012).

[11] K. Uchida, S. Takahashi, K. Harii, J. Ieda, W. Koshibae, K. Ando, S. Maekawa, and E. Saitoh, Nature (London) **455**, 778 (2008).

[12] J. Xiao, G. E. W. Bauer, K.-c. Uchida, E. Saitoh, and S. Maekawa, Phys. Rev. B **81**, 214418 (2010).

[13] I. A. Campbell and A. Fert, in *Handbook of Ferromagnetic Materials*, edited by E. P. Wohlfarth, Vol. 3 (Elsevier, 1982), pp. 747–804.

[14] J. Shi, S. Parkin, L. Xing, and M. Salamon, J. Magn. Magn. Mater. **125**, L251 (1993).

[15] S. A. Baily, M. B. Salamon, and W. Oepts, J. Appl. Phys. **87**, 4855 (2000).

[16] L. Gravier, A. Fabian, A. Rudolf, A. Cachin, J.-E. Wegrowe, and J.-P. Ansermet, J. Magn. Magn. Mater. **271**, 153 (2004).

[17] L. Gravier, S. Serrano-Guisan, F. Reuse, and J. P. Ansermet, Phys. Rev. B **73**, 024419 (2006).

[18] M. C. Cadeville and J. Roussel, J. Phys. F **1**, 686 (1971).

[19] F. L. Bakker, J. Flipse, and B. J. van Wees, J. Appl. Phys. **111**, 084306 (2012).

[20] D. MacDonald, *Thermoelectricity: An Introduction to the Principles, Dover Books on Physics* (Dover Publications, 2006).

[21] A. Slachter, F. L. Bakker, and B. J. van Wees, Phys. Rev. B **84**, 174408 (2011).

[22] F. L. Bakker, A. Slachter, J.-P. Adam, and B. J. van Wees, Phys. Rev. Lett. **105**, 136601 (2010).

[23] J. R. J. Soulen, M. S. Osofsky, B. Nadgorny, T. Ambrose, P. Broussard, S. F. Cheng, J. Byers, C. T. Tanaka, J. Nowack, J. S. Moodera, G. Laprade, A. Barry, and M. D. Coey, J. Appl. Phys. **85**, 4589 (1999).

[24] J. Bass and W. P. Pratt, J. Phys.: Condens. Matter **19**, 183201 (2007).

[25] E. Tsymbal and I. Zutic, *Handbook of Spin Transport and Magnetism* (CRC Press, 2011).

[26] E. Y. Tsymbal, D. G. Pettifor, J. Shi, and M. B. Salamon, Phys. Rev. B **59**, 8371 (1999).

[27] A. Slachter, F. L. Bakker, and B. J. van Wees, Phys. Rev. B **84**, 020412 (2011).

[28] S. Dubois, L. Piraux, J. M. George, K. Ounadjela, J. L. Duvail, and A. Fert, Phys. Rev. B **60**, 477 (1999).